Polarimetry and Interferometry Applications

Wolfgang Keydel
Microwaves and Radar Institute
German Aerospace Research Centre (DLR), Oberpfaffenhofen
Contact Address:
Mittelfeld 4
D-82229 Hechendorf
Germany
E-mail: wolfgang.keydel@dlr.de

Abstract

Based on the foregoing lectures respective applications of both Polarimetry and Interferometry will be presented. From he large palette of possibilities which includes global mapping with space borne SAR and the establishment of digital terrain models with high accuracy, observation and to some extent prediction and forecast of natural disasters (involving landslides caused by earthquakes ore avalanches, volcanic eruptions, fires, floods, terrain resurfacing, followed by a period of recovery, etc.), measurement of soil moisture, quantitative tree height determination and ground topography mapping and, as a consequence, the respective biomass estimation. Along track measurements allow moving target indication and traffic monitoring by evaluation of the position, time, velocity and direction of moving vehicles ore finding traffic jams respectively. The question of optmal radar centre frequencies for different applications is addressed also.
.

1. Introduction

The application possibilities of SAR Interferometry and Polarimetry have been researched during the last 20 years intensively and the progress obtained is tremendous. This extremely wide interdisciplinary field is an area of intensive research up to now where to some extent the disciplines are overlapping widely. The progress is still steeply increasing and, therefore, only small parts of the whole spectrum can be treated here. Henderson and his colleagues in 1998 (Reference in the Introduction of the Lecture Series) have inventoried excellently the state of the art up to 1998. Therefore, the most examples in the following are based on publications dated from the last years.

The upcoming sections of this Lecture offer a glance into a selection of representative activities in the domains of Scientific , Commercial, and Operational Applications of Interferometry and Polarimetry. Goal is to point out exemplary some application possibilities of the Interferometric and to some extent Polarimetric techniques and systems considered and presented in the forgoing respective lectures in order to deepen and fasten the understanding and the comprehension of the auditory. However, some spotlights only can be presented here which are single lines in an extremely wide spectrum. Instead of a large and global but in any case incomplete overlook some single application tasks will be presented as examples for some large areas, and they will be explained in more detail and deepness together with respective references in order to give an impression on the work Which has to be done to come to usable products.

2. Application Areas and Specific User

User requirements and application possibilities are the driver for research and development of all SAR technique, technology and system development. Table 1 gives a glimpse on the extremely wide range of application areas and the SAR parameter which are optimal for some applications.

SAR Interferomery offers a umber of highly promising applications: the creation of land deformation maps with millimetre accuracy the generation of digital elevation models with meter accuracy,improved target recognition by creation of 3D images of targets improved land use classification by exploiting coherence

Paper presented at the RTO SET Lecture Series on "Radar Polarimetry and Interferometry", held in Brussels, Belgium, 14-15 October 2004; Washington, DC, USA, 18-19 October 2004; Ottawa, Canada, 21-22 October 2004, and published in RTO-EN-SET-081.

measurements, the measurement of current fields and moving target indication Interferometry is of economical and operational importance for constructors (e.g. because building a tunnel can cause unwanted deformation), governments (e.g. for dike monitoring), the military (e.g. for topographic maps), governments and companies creating geo-rectified SAR imagery (this needs topographic maps), etc.

SAR Polarimetry offers the maximal information an Electromagnetic Wave can carry. Therefore, for the most modern civil and military applications full polarimetric systems are required. As an example, the expectations which both, the civil and military remote sensing community has are extremely optimistic.

Parameter	Cartography	Disaster Management	Urban Mapping	Military
Frequency	L, C, X	L,C,	L, C, X	L, X
Polarization			Quad	Quad
Incidence Interval	Variable	Variable 20° - 60°	Variable 20° - 60°	Variable 20° - 60°
Spatial Resolution	3 m – 5 m		1 – 5 m	0,1 m -10 m
Swath Width	Variable	Variable 20km -350 km	40 km – 100 km	5km – 100km
Revisit Time	1 Year Application request	1 hr – 1 day	Yearly	1 hr –1 day
Data access	regularly	real	Regularly	Real Tme

Tab. 1b www.iaanet.org/symp/berlin/IAA-B4-0203.pdf

Parameter	Agriculture	Forestry	Geology	Hydrology	Oceanography
Frequency	L,C	L, C, X	L, C, X	L, C, X	L,C
Incidence Interval	25° – 45°	20° -45°	20° -60°	20°- 45°	20° -45°
Spatial Resolution	3m-30m	10 m	3m – 10m	3m – 10m	30 m-1 km
Swath Width	30 km	Variable	Variable 40 km – 100 km	Variable 100 km	Variable 25 km-350 km
Revisit Time	≤ 15 days		Seasonal	10 days – 15 days	1 day
Data access	Real Time	Regularly	Regularly	Regularly	Real Time
Additional		Tomography			Raw Data

Tab. 1a www.iaanet.org/symp/berlin/IAA-B4-0203.pdf

Polarization will improve ice detection and classification, man made target detection and classification, crop monitoring and clasification etc.. Commercial aspects are widely in the foreground also.

2.1 Military Use of Interferometry and Polarimetry

"The war is father of everything", unfortunately, this sentence holds especially for the development of radar techniques technology and systems and all the application areas. The development of Interferometry and Polarimetry has been driven intensively by military requirements. Target detection, recognition, identification and classification are put into the fore ground mostly, and for these tasks the full polarimetric information is indispensable. The polarimetric decomposition theorems are excellently suited for target exploration especially for targets hidden under vegetation layers due to foliage penetration capability of dm-waves etc. However, military reconnaissance systems have the task to "assist the military leaders in the early detection of crisis prevention and crisis management efforts, support the top military leadership to plan and prepare military operations and support deployed forces in the timely collection of current intelligence information".(Col. F. Kriegel on "European Satellites for Security" in Brussels, June 2002), and for tactical as well as for strategic consideration it is one of the biggest tasks to get things timely, safely and efficiently at the battlefield.Therefore, there is no faculty mentioned in Table 1 which has no

Figure 1a: HH polarization image showing enhanced ice-type information.

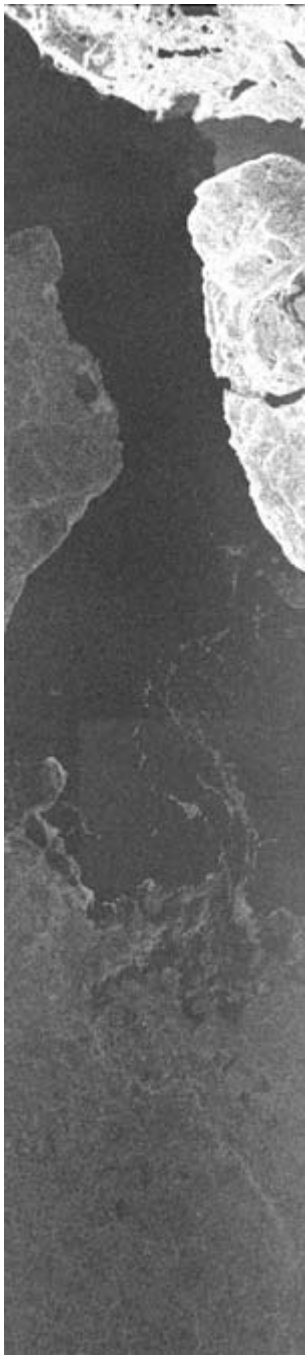

Figure 1b: HV polarization image showing enhanced ice-edge information.

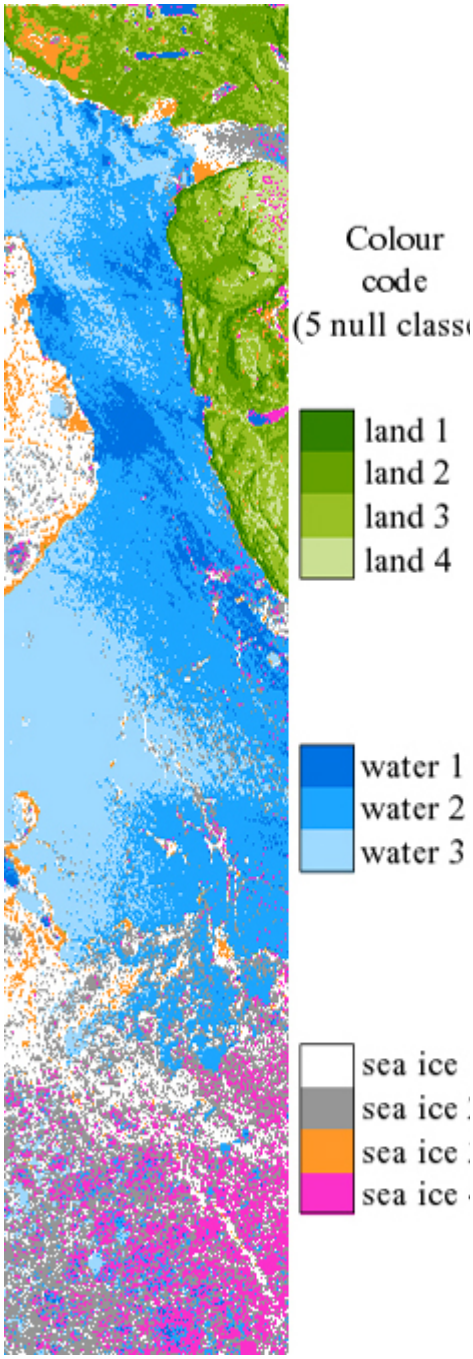

Figure 1c: H/A/a Maximum Likelihood classification results after five iterations.

meaning for military applications and all topics mentioned above are more or less relevant for military applications.

Remote Sensing can help in collecting terrain information like engineering resources, trafficability, obstacles, visibility, camouflage, concealment potential, information on camping ground, water supply source etc. All information should be regularly updated for the military purposes in required short time which can not be possible by manual process. However, systems mounted on aircrafts, UAV's, and satellites as well will allow an actual updating of already existing maps or an establishing of new feature maps as well in real time. As an example, military topographic maps are most important for terrain evaluation. Aircraft

and Helicopter missions in mountainous ore even hilly terrain can be supported in advance or during the mission if an accurate DEM of the respective area is available. Soil moisture maps can help to identify the best way for off road troop movements etc. DEM's are necessary also for establishing Communication links etc. The fact that the US NIMA has financed the SRTM mission illuminates the importance of digital elevation models for military purposes.

3. Polarization Application for SRTM ScanSAR Technique

Full coverage of the Earth with SRTM was possible in the 10 day mission by operating the radar in two two-beam ScanSAR modes, one with vertical polarization, and the other with horizontal polarization. The four beams together covered about a 225 km ground swath. The swath of the additional X-SAR was embedded at the border between the last two scans. The geometry is sketched in Fig3.1.ScanSAR, principally, achieves a large swath coverage, ~ 225 km ground range for the SRTM case, by periodically steering -on the fly- the antenna pointing towards different elevation angles in repeated stepwise fashion. Such way of operation causes a loss of data in ScanSAR against the Strip map mode. This data loss is proportional to the number of sub-swaths. The loss of data with respect to the full resolution Strip Map Mode using one sub-swath only over the whole scene length causes a proportional loss in the azimuth resolution due to the non-acquired pulses. This is what ScanSAR trades off for getting an increased range coverage. A swath extension using four sub-swaths extends the swath width but reduces the azimuth resolution by a factor of four. By exploiting the polarimetric capability of SRTM two sub-swaths have been illuminated at a time which were principally independent due to the use of two linear orthogonal polarizations for two pais of scans. Hence, a ScanSAR duty cycle of 1:2 rather than 1:4 was achieved for each sub-swath and a resolution loss decrease of 1:4 could be avoided. The scheme is depicted in Fig. 3.1.

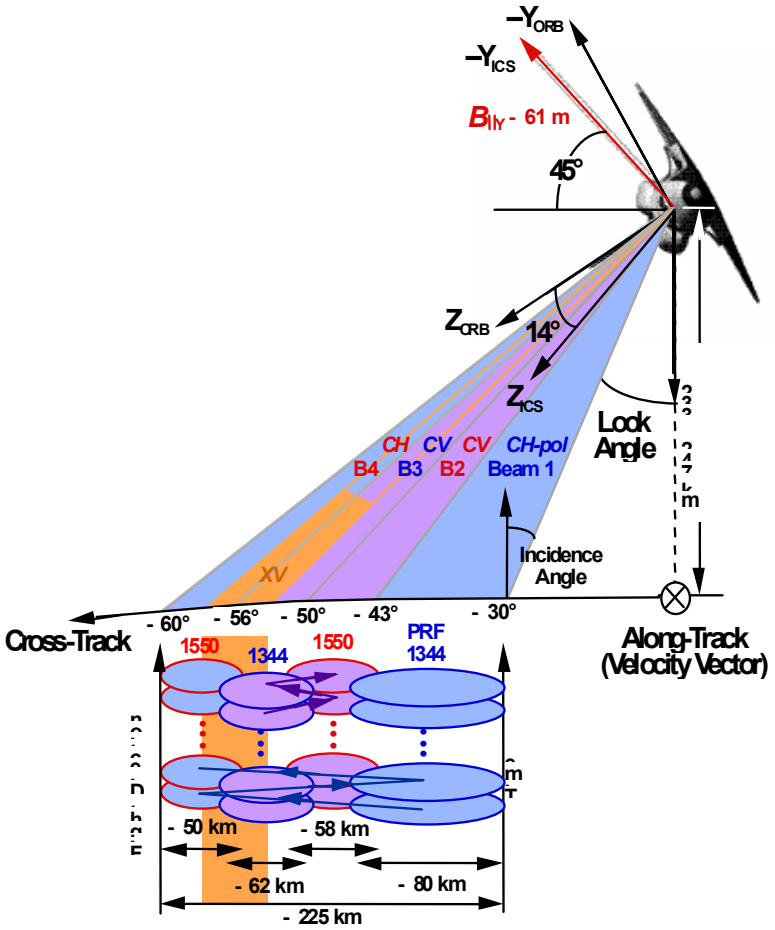

Fig.3.1 Scan scheme fort he SRTM ScanSAR-Mode in C - Band using two polarizations coded in blue and pink in order to avoid too much resolution reduction reaching an Improvement of a factor of 2 against normal Scan-SAR-Mode. Both swath and beam of X – SAR are coded in light brown.
(Image Courtesy JPL)

REFERENCE: Rosen P., S.Hensley, E. Gurrola, F. Rogez, S. Chan, J. Martin, E. Rodriguez: SRTM C-Band Topographic Data: Quality Assessments and Calibration Activities, Proc. IEEE 2001 INTERNATIONAL GEOSCIENCE AND REMOTE SENSING SYMPOSIUM, IGARSS 2001. 9 - 13 JULY 2001, University of New South Wales, Sydney, Australia(CD-ROM)

4. Tomography for Forest Applications

The inversion of geophysical parameters of a volumetric target from conventional 2-D SAR images leads in several cases to ambiguous classification results. Because several different scattering effects from different heights are mixed in the resolution cell, a reliable inversion is not always possible, even using multi-frequency and polarimetric data. The capability of SAR tomography to resolve the backscattering contributions coming from different heights can be used to improve the inversion of geophysical parameters in SAR imaging. For surface and point scatterers having no height distribution, the tomographic imaging leads to the same results as conventional interferometric SAR imaging.

In the scope of future activities, the potential for many applications will be assessed like the estimation of the ground topography, the biomass, vitality, and the height of vegetated areas and also the detection and positioning of covered objects. Furthermore, SAR tomography can contribute to solve with an improved reliability several inversion problems like the estimation of the soil roughness and humidity, ice thickness and humidity, and many other classical applications requiring an image classification. Even misinterpretations in SAR images caused by layover and foreshortening effects may be solved by tomographic SAR imaging due to the capability to have a height resolution.

It must be mentioned that SAR tomography for topographic mapping is affected in a different way than in traditional SAR interferometry by the errors caused by an imprecise tilt angle value, i.e., inaccurate knowledge of the roll angle. This means that SAR tomography can also be used for accurate terrain topographic mapping. In the present case, the achieved terrain height resolution was 3 m..

In the case of digital elevation models of forestry areas, it is normally desired to estimate the ground topography and not the top of the vegetation layer. However, even in a longer wavelength like the L-band, a significant contribution of the backscattering is occurring in the crown. Since for the traditional SAR interferometry only the total phase center of all scattering effects is relevant, the estimated height would be clearly above the ground level. With SAR tomography, it is possible to separate the ground backscattering in the forest and to estimate a height only from signal contributions related to it.

As far as the measurement of the biomass or the stem volume over forestry areas is concerned, a strong correlation between the backscattering amplitude and the present biomass has been shown in the case of conventional 2-D SAR remote sensing. However there exists the problem, that for L- and P-band a saturation is already reached for a relatively small biomass. This is due to strong backscattering contributions in the crown of the trees, which are not related to the biomass, but are still significantly strong (even in P-band). Until now, only VHF-SAR has been suitable to do reasonable measurements over forest with a density greater than 200 tons/ha (Smith and Ulander,2000). On the other hand, the VHF frequency range has the disadvantage of being inaccurate in the estimation of biomass values lower than 100 tons/ha. SAR tomography allows to estimate the backscatter contribution of the crown and to separate it from the other scattering components. The crown contribution can be used to calculate the attenuation occurred in the crown and to correct the double-bounce contribution from the stems. In this way, it should be possible to circumvent the saturation problem in wavelengths like L- and P-band. This will be considered in our future experiments.

Fig. 4.1 shows the results obtained with the first demonstration of airborne SAR Tomography using L-Band data ((Reigber, Moreira, 2000)

In the right part of the image in Fig. 4.1, a flat meadow appears as a nearly horizontal line. Its real topographic height is equivalent to the measured height. Slightly above the ground level, the strong echo of a corner reflector is visible in the right middle of the image. A little bit more to the left appears the roof of the building several meters above the ground level. From the difference between the height of surrounding ground level and the height of the roof the height of the building can be estimated and validated with the real one («13 m). Of special interest is the spruce forest. Here, the crown and the underlying ground appears bright in the slices obtained in

HH and VV polarization. In the cross-polar channel, only the crown is visible. This is a result of the different scattering mechanism contributions occurring in this kind of volumetric target.

1. Double Bounce*:* This backscattering contribution appears due to the double bounce scattering mechanism between the tree trunks and ground level. This contribution has its scattering phase center on the ground and is not present in the cross-polar channels.

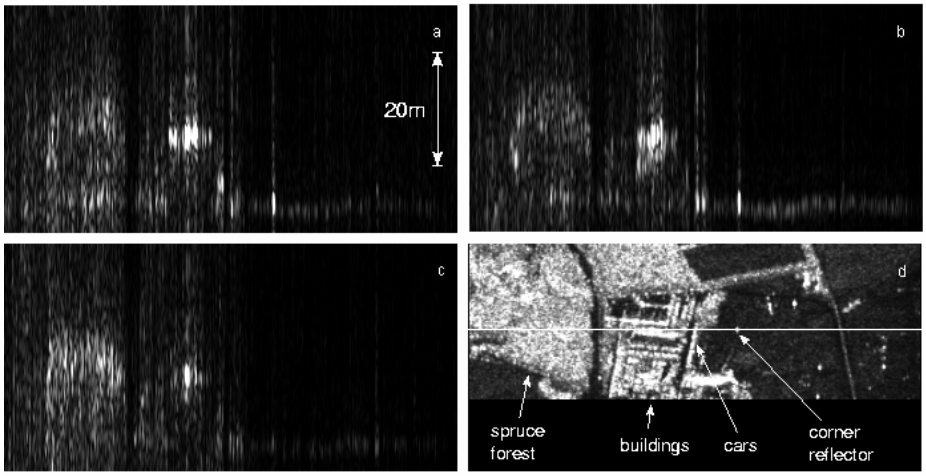

Fig.4.1: Tomography for Scattering Analysis. Different scattering mechanisms along the white line at different altitudes at different polarizations.a:HH; b:VV; c: HV. d: measurement path. The buildings roof is bright, The bright HH and VV single bounce is the corner reflector,double bounces happen at parts of the buildigs roof and at the lower parts of trunks, in tree crowns & under story volume scattering dominates.(Reigber 1999)

2. Volume Scatter. A second backscattering contribution is observed in all channels from the randomly oriented needles in the crown. The apparently stronger contribution in the HV polarization is just caused by an amplitude dynamic adjustment carried out for optimizing the contrast of the image.
The differences in height between these two different scattering mechanisms allow to estimate the height of the forest. Comparing the forest height visible in the tomographic slices with hypsometric ground truth measurements, [Ulbricht, 2000], a good agreement between both heights can be observed.

A comparison of the azimuth slices obtained in different polarizations shows several differences. But additionally to these amplitude images also the phase relations between the polarizations contain valuable information about the backscattering process. From the azimuth slices presented in Fig. 4.1 the polarimetric scattering matrices can be calculated. These scattering matrices are obtained in the HH/VV-basis and can be transformed to the Pauli-basis by a target decomposition [Cloude and Pottier, 1996]. The advantage of the Pauli-basis lies in the strong relationship between the elements of the polarimetric scattering matrix in this basis to three basic scattering mechanisms. The first scattering mechanism of Pauli-matrix contains the echo of isotropic odd-bounce scatterers, like flat surfaces or trihedral corner reflectors. The second is related to isotropic even-bounce scattering, especially double bounce. The third one corresponds to isotropic even-bounce scattering with an orientation rotated by $\pi/4$, normally occurring in the case of random volume scattering and on double bounce targets whose axis is rotated to the line-of-sight direction (e.g., dihedral corner reflectors, in realiy fences for instance) with a rotation of 45°.
The result of the Pauli-decomposition is shown in Fig. 5 of the Introduction Chapter of this lecture Series. It demonstrates that the proposed tomographic processing with ambiguity suppression preserves the full polarimetric information present in amplitude and phase of the data. The corner reflector on the right side appears in blue coming from the triple-bounce scattering occurring here. A little bit more to the left, we find a red spot at ground level related to double-bounce scattering coming from the cars parked in this area. The roof of the

building produces a mixture of odd and even bounce scattering, but have nearly no cross-polar echo except of a bright spot in the middle of the building that is strong and almost equal in all polarizations. In the spruce forest, we can now clearly identify the type of the different scattering mechanisms in the height direction. The red color of the ground level indicates that the echo

REFERENCES:
Cloude S. R. and E. Pottier, "A review of target decomposition theorems in radar polarimetry," *IEEE Trans. Geosci. Remote Sensing,* vol. 34. pp. 498-518, Mar. 1996.
Reigber, A., Moreira, A., First Demonstration of Airborne SAR Tomography using Multibaseline L-Band Data. IEEE Transactions on Geoscience and Remote Sensing, vol 38. No. 5, Sept: 2000
Smith G. and L. M. H. Ulander, "A model relating VHP-band backscatter to forest stem volume," *IEEE Trans. Geosci. Remote Sensing,* vol. 38, Mar. 2000
Ulbricht A., "Flugzeuggetragenene repeat-pass interferometrie mit dem E-SAR," Ludwig-Maximilian Univ. Munchen, Miinchen, Germany, 2000.

5. Mining Induced Subsidence by means of Differential SAR- and Permanent Scattering Interferometry

Differential Interferometry using permanent scatterers as reference points has been used for the determination of subsidence effect caused by ground water withdrawal in a brown coal mining area of the lower Rhine Embayment in Germany (Kircher, M. 2003)

The main objective, however, was to clarify the correlation between ground water withdrawal, tectonics and subsidence on the surface by means of two remote sensing methods, the differential SAR interferometry and the Permanent Scatterer technique. The results of both methods are compared among each other and to the ground measurements

The effect of subsidence in the brown coal area is indirectly caused by surface mining. To provide brown coal mining in open cast pits, the groundwater table has to be lowered below the surface mining level. This is guaranteed by using pumping stations, which extract the groundwater around the mining area. The slow groundwater stream causes a total withdrawal. These effects result in depressions around the mining areas. Mining induced subsidence shows significant amounts of motion. The changes by drawdown occur in a range of 10 years. The motion rates range from some millimetres to some decimetres per measure interval [1]. The dependency between subsidence and drawdown in the area of investigation is about 1: 3000, which means 1 m drawdown leads to 1-3 mm subsidence [2].

By using the D-InSAR method, 28 ERS-1/-2 scenes were registered to the same master image. Initially two complex SAR scenes (master and slave) have to be co-registered and spectrally filtered. For the application of the Permanent Scatterer technique 39 interferograms have been computed covering the period May 1995 - December 2000. For both applications the processing Systems of DLR have been used.

The ERS scenes had perpendicular baselines from 23 m up to 1158 m. The largest perpendicular baseline where fringes could be generated, was about 500 m. In 17 of the 28 interferograms computed by the D-InSAR method, concentric fringes can be seen, ideally forming an ellipse, as shown in the centre of Fig. 5.1. One fringe is equal to 28 mm of movement in the line of sight to the sensor. The time series of the differential interferograms (Fig. 5. 2) shows a nearly linear motion tendency. Between May 1995 and December 2000 the area affected by groundwater withdrawal sank continuously with a rate of estimated 5 cm/year. This value corresponds very well to the ground measurements made by levelling of the land surveying office NRW, Germany.

In addition to the D-InSAR technique the Permanent Scatterer technique was used also for more point wise information. About 11.000 permanent scatterers were identified in the area of investigation. For the estimation of the selected points a reference network was built.

A relation between the PS (Fig.5. 3) and the coherent phase (Fig. 5.1) can be observed. The estimation for the subsidence rate of each permanent scatterer (Fig.5. 3) shows equal values like the differential interferograms and the ground measurements.

All data and information (interferograms, ground measurements, PS, air views, thematic maps etc.) have been saved in a GIS data base for a better handling and to intersect and compare the data in a better way.

Contrary to other areas investigated by PS [5] [6], the area is dominated by intensive agricultural use and open mine pits. Therefore less long time stable back scatterers exist. The resulting problem is that the basis for the interpolation of the PS is based on less back scatterers. So all PS have to be chosen very carefully, because each point has more influence on the interpolation. The estimated PS values show a faster movement in the centre of the subsidence (see colours in fig. 5), as well the ground truth map of the land surveying office (fig. 2). As expected this motion tendency would appear in the DInSAR interferogram as concentric fringes that increase to the centre of the ellipse. In just 2 of 28 long-time interferograms generated by D-InSAR such fringe pattern with increasing fringes to the centre of the n subsidence funnel are visible. The relative unsatisfying visible spatial resolution in terms of the motion is due to residual phase noise of the differential interferograms. That leads to the conclusion, that the spatial resolution of the DInSAR can be supported by the PS techniques.

The result of the D-InSAR time series is a mean subsidence rate of 5 cm/ year. So the time resolution of both methods is very satisfying. The time resolution of the investigated 5 years (1995-2000) shows a quasi linear motion. One reason for the linearity of the subsidence can be found in the underground. The drawdown area consists in gravel and clay layers. With the first pumping event in the 1950s, the clay was relatively fast dewatered, while the water in the gravel layer (aquifer) slower leaks and the layer compacts continuously during a long time period [7]. The observed subsidence takes place in that long period of compaction.
The the D-INSAR method as well as the PSI technique lead to the same subsidence rates of about 5 cm/year. Even over a time span of 1401 days reliable results were achieved with both methods.The estimated values could be verified by ground measurements of the land surveying office NRB, Germany.

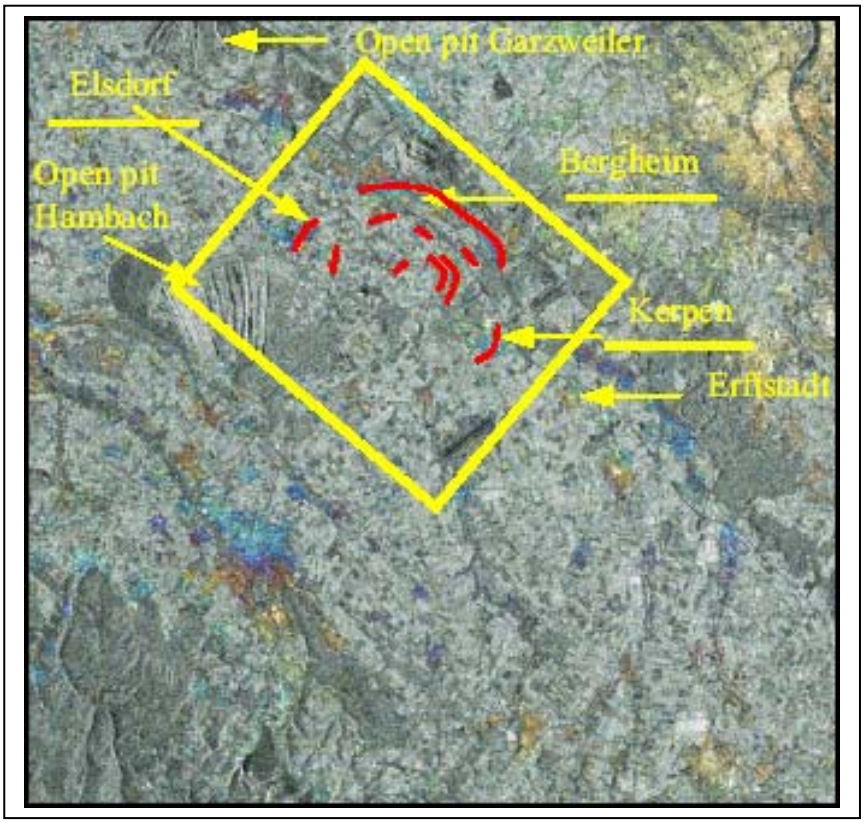

Fig. 5.1 Differential Interferogramm with amplitude overlay

The first 17 (D-InSAR) interferograms show a quasi linear subsidence. The linearity of the motion is advantageous concerning the assumption that currently is made by the Permanent Scatterer method.
By creating a GIS data base with all available data, the handling and the interpretation by intersecting different information will be more comfortable.

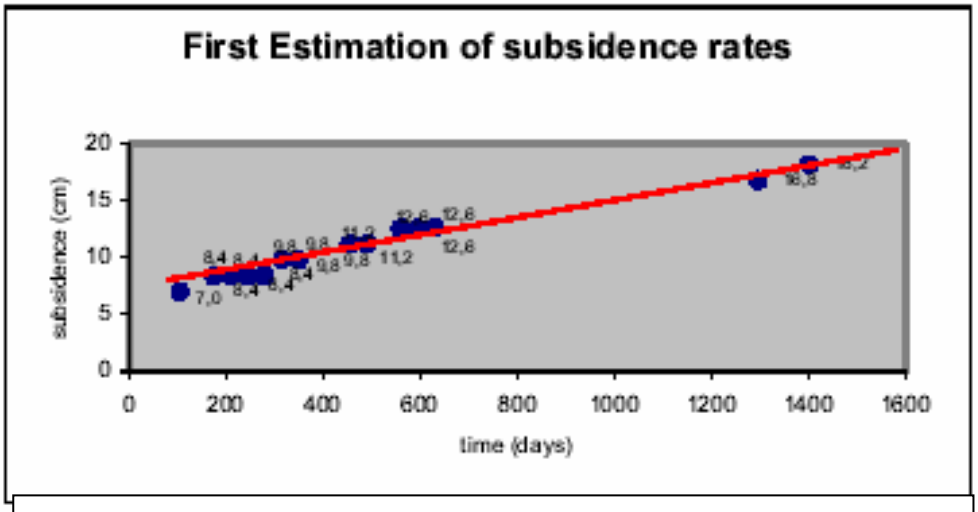

Fig.5.2 time series of an Differential Interferogram

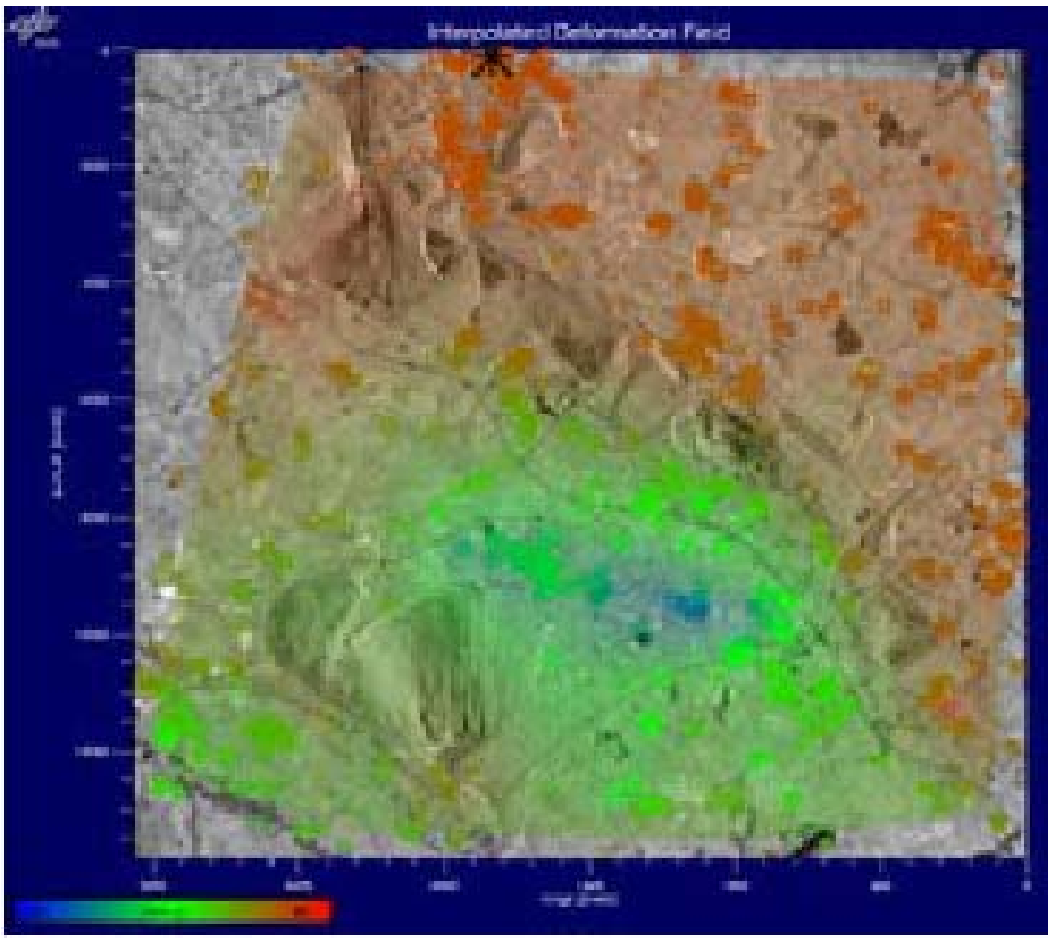

Fig.5.3 Example: estimated subsidence map, ± 4cm from blue to red.

REFERENCES
This section is based mainly on Kircher, M., A. Roth, N.Adam, B. Kampes, H. J. Neugebauer, Remote Sensing Observation of Mining Induced Subsidence by means of differential SAR-Interferometry , IGARSS 2003, which contents the following references.
[1] KIRCHER M., H.J. NEUGEBAUER AND B. RABUS, "Observation and Interpretation of Mining Induced Subsidence with Permanent Scatterers", Proc. Fall Meeting AGU 2002, San Francisco, 6-10 December 2002.
[2] W. SCHAEFER, "Bodenbewegungen und Bergschadensregulierung im Rheinischen Braunkohlerevier", DMV-Tagung, Cottbus 1999.
[3] A. FERRETTI, C. PRATI AND F. ROCCA, "Permanent Scatterer in SAR Interferometry", IEEE TGARS 1999, June 2000
[4] ADAM N . B. Kampes, "Permanent Scatterer: Software Documentation",DLR-IMF internal TNs, 2002
[5] A. FERRETTI, C. PRATI AND F. ROCCA, "Analysis of Permanent Scatterers in SAR Interferometry", IEEE 2000,
[6] A. FERRETTI, F. FERUCCI, C. PRATI AND F. ROCCA, "SAR Analysis of Building Collapse by means of the Permanent Scatterer Techniques", IEEE 2000"
[7] K. TERZAGHI, "Theoretical Soil Mechanics", Wiley New York 1943

6. Buildings determination with SAR interferometry

High resolution SAR systems can be used to create 3-D maps of man-made structures such as buildings, and to populate herewith novel 3-D Geographic Information Systems (GIS) using terrain elevation data produced by the interferometric radar component in combination with the grey value images and their object shadows. The accuracy of buildings mapped from a sensor with 30 cm pixels is at about ± 3 pixels or ±1 m. 3D models of buildings can be established using each building's footprint. An elevation measurement can be computed from the shadow lengths. This approach results in an independent estimate of the building's shapes. However, it is necessary to employ more than a single radar imaging data set to map buildings.

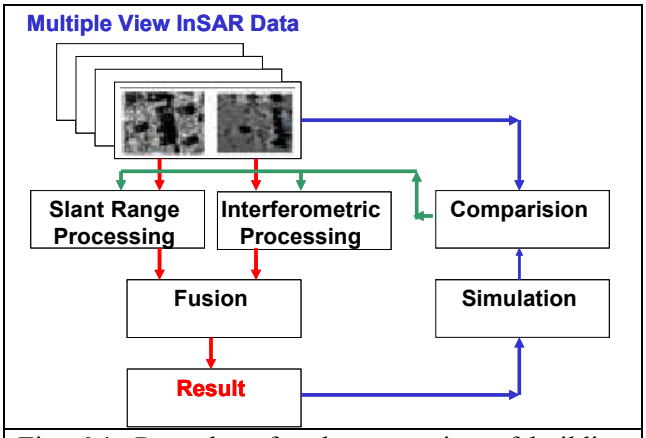

Fig. 6.1: Procedure for the extraction of building modelsfrom a combination of SAR images and associated interferometric data [6] (Bolter, 2001).

The procedure is sketched in Fig.6.1. After an analysis of the interferometric terrain elevation data, exploiting the redundancy in the multiple data sets to arrive at a single elevation map, the vertical objects filter. The resulting vertical candidate objects are then subjected to a classification based on the coherence values of the interferometric data sets, separating the objects into vegetation and buildings. This approach was developed and validated for the combination of four views.

Building candidates are being selected or filtered by a morphological operator. Finally a minimum bounding rectangle is computed for each vertical building blob, and a single elevation is assigned to each rectangle, resulting in a purely interferometric estimate of each building's shape. In parallel, the slant range gray value images are being processed as well. Shadows are segmented using some simple rules about shadows. Shadow boundaries from multiple views are combined to produce estimates of each building's footprint. An elevation measurement can be computed from the shadow lengths. This approach results in an independent estimate of the building's shapes.

The footprints of shadow-based buildings are more accurate from interferometry and height estimates are more accurate from interferometry. Combining the two data sets leads to a single result that is now subject to verification by simulation. The building models are input to an image simulator. The result is being compared to the gray value images. Mismatches serve to flag errors in the measurements. The correction of those errors requires a strategy employing the radar image's phenomenology. For example, lay-over regions

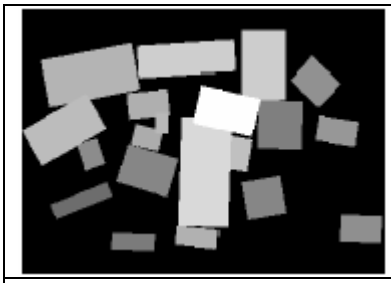

(a) bottom view

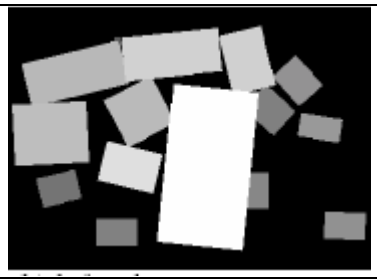

(b) left + bottom

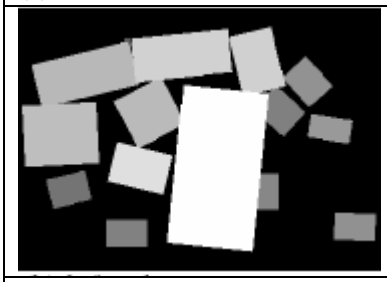

(c) left+ right+bottom

Fig. 6. 2: Resulting Minimum Bounding Rectangles fit to point clouds detected automatically from maximum combined height map for different view combinations.The area covers approximately 200 x 150 m².

can be identified in the interferometric and in the grey value data, and these layover regions can be used to improve the accuracy and robustness of the individual measurements.

The final model of the 15 buildings was shown in [6] (Bolter, 2001). The accuracy of the building heights is abut 1.0 m rrms, with the error due to the missing church steeple disregarded. The height maps appear smoother and especially shadow areas are reduced significantly as more views are added. The method of building extraction has been applied to each of the combined elevation maps. Figure 6.2 illustrates the resulting bounding boxes for the detected m buildings from a single view (a) and the combination of two (b) and three views (c). Note that as fewer images are being used, the detection of buildings deteriorates, for example detecting 19 buildings when 15 are present!

Height measurements can be obtained from segmented shadows for different view combinations, and the results are shown in Table 6.1 for the resulting maximum height error, computed as an rms-error over the 15 buildings. Because less than half of the buildings can be recovered from a single view, the resulting height measurements are quite poor for single views. But the error decreases when multiple views are added.

The building's outlines for the entire scene can be reconstructed from different view combinations. These building's outlines can be quite fuzzy, various gaps and outliers may exist due to noise still present in the segmented shadow areas. In single views occlusions will be a problem, when adjacent buildings interfere with the shadow regions of the actual building. Another problem occurs at the endpoints of each wall, where layover effects superimpose shadow areas. In order to fit building models to this resulting point cloud, the point clouds have to be

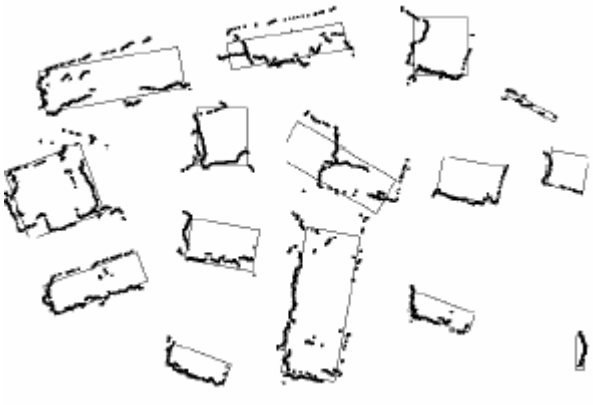

Fig. 6.3: Footprints from shadows, reconstructed from two perpendicular views, right + top. Overlaid are the computed optimum rectangles to fit the Point clouds.The area covers approximately 200 m x 150 m

Especially in the case of two perpendicular views some cases of insufficient wall information occur. Therefore the calculation of the optimum rectangle fails in two cases. With respect to shadow reconstruction, opposite views should be preferred if only two views are captured. The conclusion can be drawn that the area measurements from shadows are more accurate than they are from interferometry.

Table 6.1 illustrates the accuracy if only one, two, three or four images are being used (l=left, r=right, b=bottom, t=top). An automated approach to extract building models uses the interferometric measurements and the shadow boundaries from radar gray value images. The resulting elevation accuracy is about 1 m. The accuracy of the building footprints is more accurately determined from shadow boundaries with uncertainties in the range of $\pm$30m ^{2}. Single radar images do not support an accurate extraction of building models. At least two separate images are needed from opposite sides. This affects the measurement of the area of a building's footprint more than the estimate

of building height. Of interest would be the use of interferometry presented in slant range to employ edge information. Gray value edges have also not yet been investigated. More complex models of buildings need to be provided to the analysis, so that an error such as missing the church steeple does not occur.

View Combination	Error of Areas (RMS)	Height error (RMS)	Number of detected Buildings
Bottom	± 205 m^2	± 2,1 m	21
Left + Right	± 276 m^2	± 2,6 m	12
Left + Bottom	± 422 m^2	± 1,6 m	14
Left + Right + Bottom	± 207 m^2	± 1,4 m	16
Left + Right +Top + Bottom	± 120 m^2	± 1,4 m	15

Table 6.1: Resulting rms error of area and of the maximum height, as a result of applying the automated building detection algorithms to different view combinations. “Maximum height” is used to avoid the confusion resulting from sloping roofs.

REFERENCES

This section is based mainly on Leberl F. W., Regine Bolter, From Multiple View Interferometric Radar to Building Models, Proc. EUSAR 2002 with further references

[1] R. Bolter, F. Leberl [2000]: „Phenomenology-Based and Interferometry-Guided Building Reconstruction from Multiple SAR Images“, Proceedings of EUSAR 2000, München, Germany, pp. 687-690.

[2] R. Bolter, F. Leberl [2000a]: „Detection and Recon-struction of Human Scale Features from High ResolutionInterferometric SAR Data“, Proceedings of ICPR 2000, Volume 4: Applications, Robotics Systems and Architectures, Barcelona, Spain, pp. 291-294.

[3] R. Bolter, F. Leberl [2000b]: „Shape-from-Shadow Building Reconstruction from Multiple View SAR Images“, In R. Sablatnig, Ed. Applications of 3D-Imaging and Graph-Based Modeling 2000, 24 th Workshop of the Austrian Association for PatternRecognition, Österreichische Computer Gesellschaft, Band 142, pp. 199-206.

[4] R. Bolter, Leberl F. [2000c]: „Detection and Recon-struction of Buildings from Multiple View Interferometric SAR Data“, Proceedings of IGARSS 2000, Hawaii, pp. 749-751.

[5] R. Bolter, Leberl F. [2000d]: „Fusion of Multiple View Interferometric and Slant Range SAR Data for Building Reconstruction“, EOS/SPIE Remote Sens-ing Symposium, Barcelona, 2000, Conference on SAR Image Analysis, Modeling, and Techniques III, SPIE Vol. 4173, pp. 241-250.

[6] R. Bolter [2001]: „Buildings from SAR: Detection and Reconstruction of Buildings from Multiple View High Resolution Interferometric SAR Data“, Doctoral Dissertation, Graz University of Technology.

[7] Burkhart G., Bergen Z., Carande R. [1996]: „Eleva-tion Correction and Building Extraction from Interferometric SAR Imagery“, Proceedings of IGARSS '96, pp. 659-661.

Detection and Extraction of Buildings from Inter-ferometric SAR Data“, IEEE Transactions on Geo-science and Remote Sensing, 38(1), pp. 611-618, January.

[9] K. Hoepfner & Hanson A., Riseman E. [1998]:„Recovery of Buildings Structure from SAR and IFSAR Images“, ARPA Image Understanding Workshop, Morgan-Kaufmann, pp. 559-563..

[10] K. Karner, J. Bauer, A. Klaus, F. Leberl, M. Grabner[2001]: „Virtual Habitat: Models of the Urban Outdoors“, 3 rd Int’l Workshop on Automatic Extraction of Man-Made Objects from Aerial and Space Images, 10-15 June 2001, Monte Verita, Ascona, Switzerland. Balkema Publishers, Holland, pp. 393-402.

7. Ocean Current Measurements with Along Track Interferometry

The X band interferometric SAR data acquired during the Shuttle Radar Topography Mission (SRTM) in early 2000 include phase images of ocean scenes which exhibit clear signatures of spatially varying surface currents. As an example a quantitative comparison of a SRTM-derived current field obtained from the Waddenzee area with results from KUSTWAD - which is the name of a model - will be given (R. Romeiser, 2003).

KUSTWAD is one of the so-called WAQUA / TRIWAQ based hydraulic models that are being developed is a and maintained .at the National Institute for Coastal and Marine Management ("RIKZ" in Dutch) of

Rijkswaterstaat in The Hague [3] to describe and predict the consequences of management measures in the Waddenzee area. Between others the model contains the part of the Dutch Waddenzee overflown with SRTM. t It has a curvilinear schematisation with a resolution varying from 50 m up to 2.5 km. The representation of the bottom is based on the latest available depth data.

The KUSTWAD results available for this study cover one tidal cycle on 23 March 1995, 1:00 through 14:00 UTC, with a time step of one hour. That is, the model was not applied to the specific scenario at the time of the SRTM overpass (15 February 2000, 12:34 UTC), but to another scenario about five years earlier. However, the agreement between measured and simulated current fields should usually be good at the same tidal phase. The shortest time lag between the tidal phase at the time of the SRTM overpass (3:16 hours before high water in West-Terschelling) and an available KUSTWAD current field is 20 minutes.

Figure 1 shows the line-of-sight current field derived from the SRTM data and a corresponding current field derived from the KUSTWAD result for the tidal phase 20 minutes before the SRTM overpass. The qualitative and quantitative agreement of the two datasets appears to be quite good. In particular, the topography-guided strong currents in relatively narrow channels exhibit very similar flow patterns and have very similar magnitudes.Figure 2 shows a corresponding scatter plot of SRTM derived vs. KUSTWAD-derived line-of-sight currents. The correlation coefficient between the two datasets is 0.558, the regression coefficient is 1.011, and the rms difference is 0.24 m/s. The mean difference is found to be 0.02 m/s. In view of the fact that the SRTM phases were not absolutely calibrated and that the bias of the SRTM-derived current field was manually adjusted such that the line-of-sight current becomes 0 in the vicinity of the Ijsselmeer dam [2], this is a quite good result.

To compare spatial variations in the SRTM-derived line-of-sight current field and the corresponding KUSTWAD-derived current field, correlation and regression coefficients of the differences in the two current fields on different length scales have been computed. For example, differences between pixels in the SRTM current field which are separated by 1 km were correlated with the corresponding differences between pixels in the KUSTWAD current field to obtain regression and correlation coefficients for variations on a length scale of 1 km. This analysis was performed for distances of 100 m (1 pixel length) to 10 km parallel and perpendicular to the look direction of SRTM. Results are shown in Figure 4. They indicate that the correlation and regression coefficients are almost constant down to spatial scales on the order of 1 to 2 km.

The results of the analyses indicate that the SRTM-derived line-of-sight current field agrees quite well with the corresponding KUSTWAD result down to spatial scales of 1 to 2 km. The correlation is between 0.5 and 0.7, and the regression coefficient is close to 1. In view of the fact that SRTM was not designed for current measurements and that the KUSTWAD model does not necessarily provide perfect reference data, this is a quite positive and promising result.

REFERENCEs

This sentence mainly based on. Romeiser R, Breit H, Eineder M, Runge M., Flament P, de Jong K, Vogelzang J.:Validation of SRTM-Derived Surface Currents off the Dutch Coast by Numerical Circulation Model Results, IEEE Proc. IGARSS 03, July 21-25, 2003 Toulouse, France containing the references below
[2] R. Romeiser, H. Breit, M. Eineder, and H. Runge, "Demonstration of current measurements from space by along-track SAR interferometry with SRTM data", in *Proc. 2002 International Geoscience and Remote Sensing Symposium (IGARSS 2002)*, 3 pp., Inst. of Elec. and Electron.Eng., Piscataway, N.J., USA, 2002.
[3] H.H. ten Cate, S. Hummel, and M.R.T. Roest, "An open model system for 2d/3d hydrodynamic simulations", in *Proc. Hydroinformatics 2000*, International Association of Hydraulic Engineering and Research, Madrid, Spain, 2000.
[4] M.E. Philippart and A.W. Gebraad, "Assimilating satellite altimeter data in operational sea level and storm surge forecasting", in *Proc. Second International Conference on EuroGOOS*, EuroGOOS Office, Southampton, UK, 2000.
[5] M. Verlaan, "Data assimilation for storm surge forecasting in the North Sea", in *Proc. Third International Conference on EuroGOOS*, EuroGOOS Office, Southampton, UK, 2002.

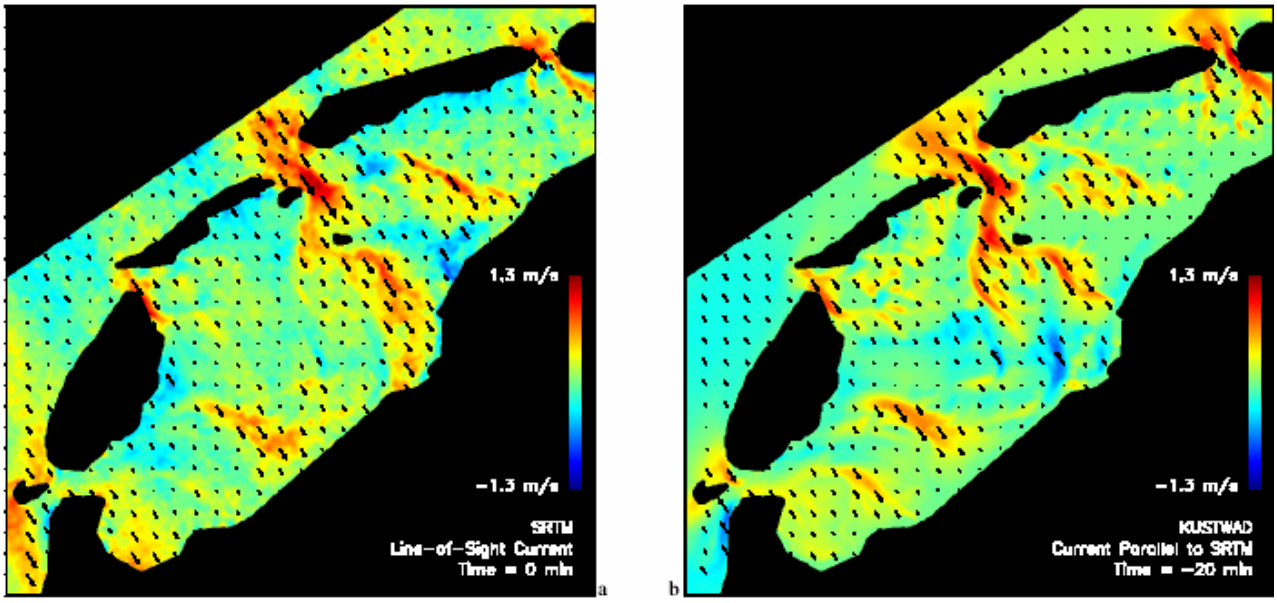

Fig.1 Line-of-sight current field in the test area as derived from the SRTM data (left) and as obtained from KUSTWAD for the tidal phase 20 minutes before the SRTM overpass (right); grid resolution is 100 m × 100 m; data points with valid currents from SRTM and KUSTWAD are shown only.

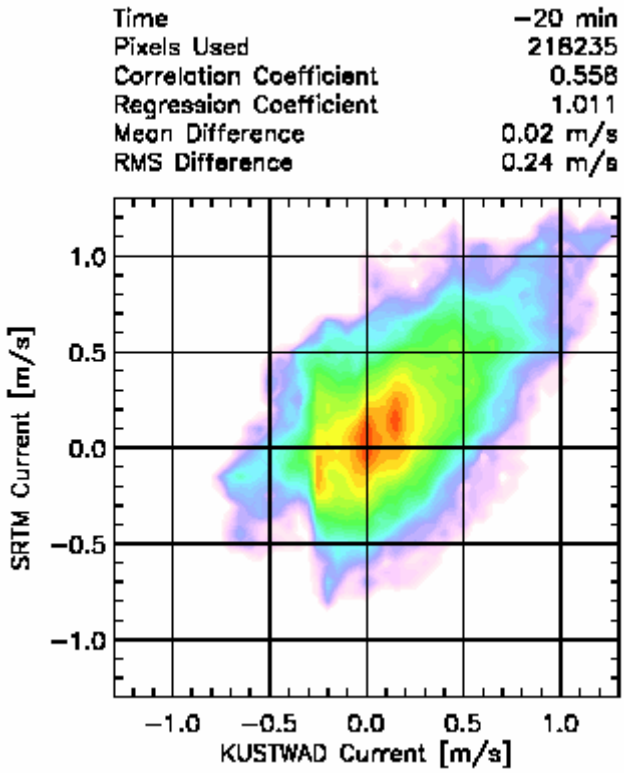

Figure 2. Scatter diagram showing the distribution of SRTM-derived vs. KUSTWAD-derived current components in the SRTM look direction, as well as corresponding statistical quantities, for the tidal phase 20 minutes before the SRTM overpass.

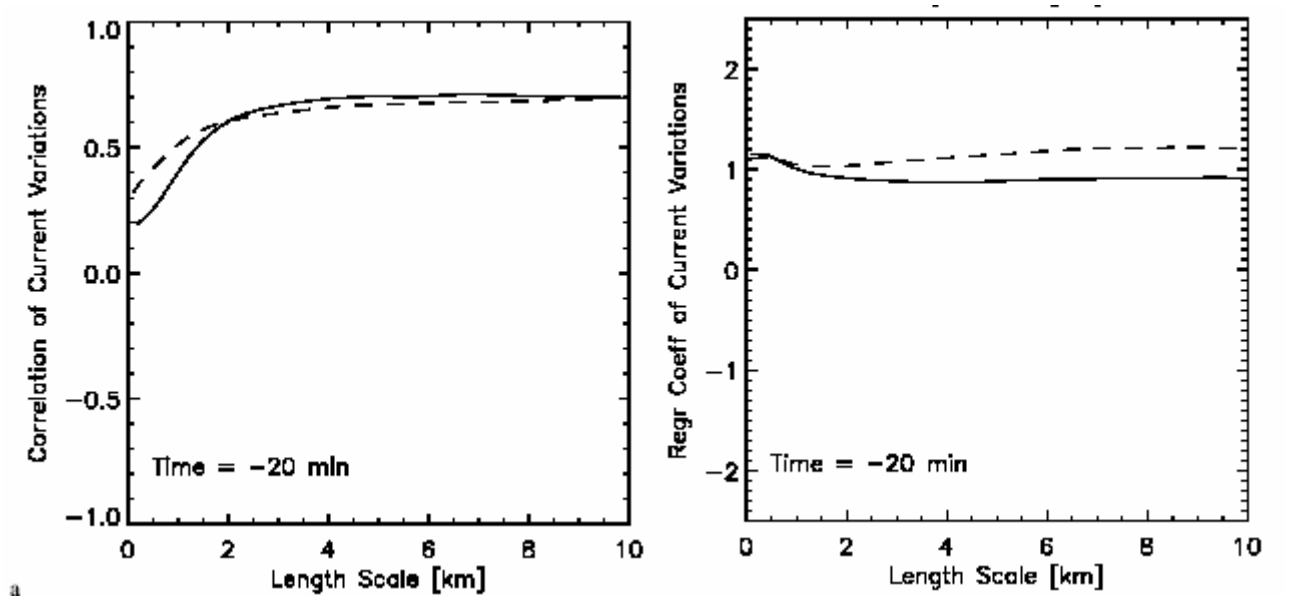

Figure3. Correlation (left) and regression coefficient (right) of variations in the SRTM and KUSTWAD currents at different spatial scales parallel (solid lines) and perpendicular (dashed lines) to the SRTM look direction.

8. Traffic Monitoring using Space-borne Along-Track Interferometry

For traffic flow monitoring and control the need for remote sensing data, acquired day and night under all weather conditions, becomes a demanding issue. Adequately designed SAR systems could be an answer [6]. As mentioned already in both the Interferometry and the Systems Chapter the SRTM had to some extent along track capability. During the Mission an experiment has been performed in order to prove principally the applicability of space-borne SAR for traffic monitoring. This will be presented here as an example for Interferometry Application Possibilities

The radial component v_r of the target velocity, relative to the line of sight, contributes an additional linear term to the target's phase history compared to the stationary case [2], [3]. Furthermore it adds to the range cell migration. In our case, a contribution of more than 8 m, half of the range resolution cell, within the aperture time would require a target motion with a radial component of more than ±200 km/h.

The tangential, along track, component v_t of the target velocity alters the Doppler rate compared to the stationary case. Commonly agreed, for phase aberrations of $\pi/4$ at both edges of the synthetic aperture, azimuth defocusing becomes significant. This limit is reached for Doppler rate mismatches higher than $1 / (4 \cdot (t_{aperture} / 2)^2) = 51$ Hz/s. For a moving target located at near range (390 km) this would impose a tangential velocity higher than

$$v_t = \pm\sqrt{(\lambda \cdot R_{target})/(8 \cdot t_{aperture}^2)} \approx \pm 2000 km/h. \qquad (1)$$

Hence, in the velocity range considered here no defocusing due to additional range migration or due to a FM-rate mismatch will occur. In the following, only the radial component will be exploited for moving target indication (MTI) and velocity estimation.

The Doppler shift caused by the additional linear phase term leads to an azimuth displacement of the focused target. The maximum unambiguous Doppler shift of ±PRF/2 corresponds to a radial target motion of $\pm \lambda/4$ (which results in a two-way distance of $\lambda/2$) from pulse to pulse. Thus, without further knowledge, v_r may be unambiguously determined from azimuth displacement in the interval of $\pm PRF \cdot \lambda/4 = \pm 47.05$ km/h. The displacement depends on the targets slant range r:

$$\Delta t_{azimuth}(r) = \frac{2 \cdot v_r}{\lambda \cdot FM(r)} \qquad (2)$$

Targets moving radially away from the sensor are displaced reverse to the flight direction.

The ATI phase [1], which computes to

$$\theta_{ATI} = (4\pi / \lambda) \cdot \Delta t_{acquisition} \cdot v_r , \qquad (3)$$

is unambiguously obtained, as long as the target moves radially less than ± λ/4 in the time between the two data acquisitions. For the time lag $t_{acquisition}$ = 0.00047 sec, v_r can be unambiguously determined in the interval of ±59.8 km/h, corresponding to $\vartheta_{ATI} = \pm\pi$.

Both velocity estimation methods are affected by wrapping and are therefore ambiguous. Since the wrapping velocity intervals for both methods are different, a two dimensional unwrapping approach can resolve the ambiguity for velocities which exceed the one dimensional maximum unambiguous velocity.

On February 18th, 2000 at 10:22 AM the Oberpfaffenhofen area was by SRTM's 109th orbit. Simultaneously, a car, equipped with both a GPS receiver and a Luneberg Lens to increase the RCS was driven on a road in across track direction.

The coherence map, a by-product of interferometric SAR processing, is a valuable data set to detect moving targets. Therefore, the one second time tick GPS measured WGS-84 car coordinates are projected into the SAR coordinates (t, r), i.e. the zero-Doppler plane. From the neighbouring one second time tick GPS

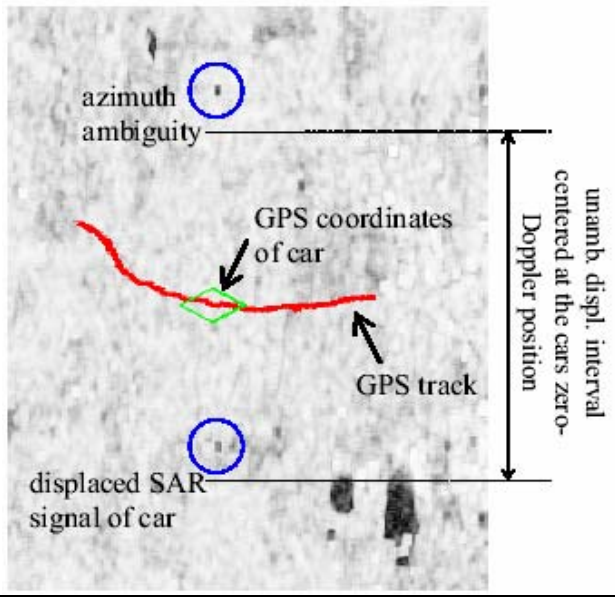

Figure 1. Coherence loss indicates the presence of a.moving target. The larger low coherent areas are Lakes (Breit et. al. , 2003)

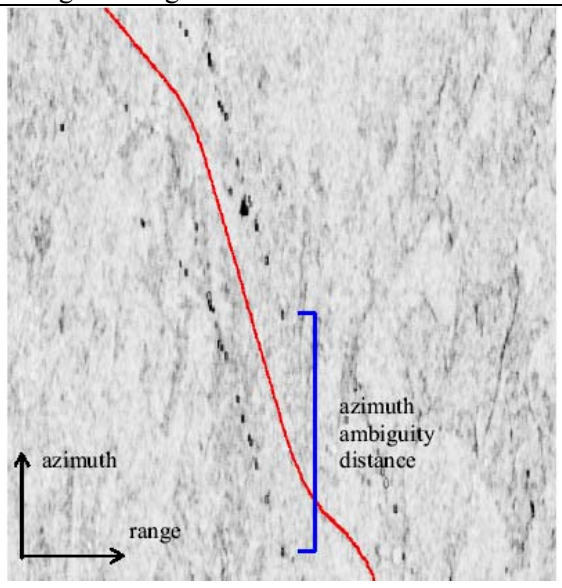

Figure 2. Coherence map featuring a 3 km long section of the Autobahn Munich – Nuremberg. The blck dots are cars displaced from the red road due to their velocities

measurements the exact car location at the time of SAR illumination is interpolated and the car heading angle is determined. Together with the incidence angle ϑ_i and the satellite heading angle satellite the car's radial velocity v_r computes to

$$v_r = |v| \cdot \sin(\theta_i) \cdot \sin(\psi_{satellite} - \psi_{car}) = 0.804 \cdot |v| \qquad (4)$$

Now the coherence loss caused by the car's radial motion induced ATI phase disturbance should be detectable within the azimuth ambiguity interval. The interval is (PRF2/FM(r)) = 324 samples wide and centered at the target's zero Doppler position. Finally the car's location is determined within the interpolated complex SAR image with sub pixel accuracy even if pixel level accuracy is sufficient due to the high sensitivity of the displacement effect. The phase is measured in the interferogram.Since the SRTM interferograms are dominated by the topographic phase, the terrain height contribution to the target's phase is estimated by averaging the phase of the surrounding samples. Table 1.summarizes the results and highlights the perfect agreement of the GPS measurements on ground and the velocity estimate derived from the azimuth displacement.

InSAR data evaluation	
Velocities resulting from measured azimuth displacement (130.6 pixel)	
radial velocity from displacement 37.9 km/h	37,9 km/h
ground velocity from displacement 47.1 km/h	47,1 km/h
Velocities resulting from ATI phase (127°)	
radial velocity from ATI phase 42.2 km/h	42,2 km/h
ground velocity from ATI phase 52.5 km/h	52,5 km/h
Velocity resulting from GPS measurement	
ground velocity	48.33 km/h

TABLE 1. Results of the Validation Experiment comparing the tree measurement methods

It is evident that the velocity of a car can bee measured exactly from space even without the application of specialized MTI SAR processing algorithms. The coherence map of the ATI phase allows reasonable moving target identification. Additionally the ATI phase itself enables a two dimensional resolving of the velocity ambiguity. The azimuth displacement, which is exploited for the precise determination of the radial velocity, is measured as the distance between the misplaced signal occurrence in the SAR data and the GPS derived zero-Doppler position. Thus, the use of a geographical information system (GIS) seams to be indispensable in order to precisely determine the azimuth displacement from the highways and in order to determine the highway orientations, i.e. the car track angle car. Figure 2. shows that trucks which are misplaced along both sides of the motorway can be identified in the coherence image.

The upcoming TerraSAR-X mission will be predestined for traffic monitoring applications due to the sensor's extremely high resolution imaging capabilities in combination with its ATI mode, enabled by the optional dual receive antenna configuration [6]. However, for that purpose al least a near real time procedure is necessary with very short revisit times. A sytem like SAR-Lupe could be a solution.

REFERENCES

This sentence mainly is an extended summary of Breit H., M. Eineder, J. Holzner, H. Runge, R. Bamler: Traffic Monitoring using SRTM Along-Track Interferometry, IEEE Proc. IGARSS 03, July 21-25, 2003 Toulouse, France containing the references below

[1] R. Bamler and P. Hartl, "Synthetic aperture radar interferometry", *Inverse Problems 14*, 1998.

[2] J. R. Moreira and W. Keydel, "A new MTI –SAR approach using the reflectivity displacement method", *IEEE Transactions on Geoscience and Remote Sensing.*, vol. 33, no. 5, pp. 1238-1244, 1995.

[3] J. K. Jao, "Theory of Synthetic Aperture Radar Imaging of a Moving Target", *IEEE Trans. Geosci. Remote Sensing*, vol. 39, no. 9, pp. 1984- 1992, 2001.

[4] A. A. Thompson and C. E. Livingstone, "Moving target performance forRADARSAT-2", *IGARSS 2000*, Honolulu.

[5] N. Adam, M. Eineder, H. Breit, S. Suchandt, "Shuttle Radar Topography Mission (SRTM): DLR's Interferometric SAR Processor for the Generation of a Global Digital Elevation Model", *Sec. Int. Workshop on ERS SAR Interferometry FRINGE'99*, Liège, Belgium, 1999.

[6] J. Mittermayer and H. Runge, “Conceptual Studies for exploiting the TerraSAR-X dual receive antenna”, *IGARSS 2003*, Toulouse.
[7] R. Romeiser, H. Breit, M. Eineder, H. Runge, "Demonstration of current measurements from space by along-track SAR interferometry with SRTM data", *IGARSS 2002*, Toronto.

9. Interpretation of Coherence Maps based on Multi Frequency Two Pass Interferometry

The SIR-C/X-SAR mission offered for the first time the possibility to study multi frequency interferometric satellite SAR data. Detailed comparison of these multi frequency data over different terrain types provides insights into the wavelength-dependent effects of penetration and scattering, and allows useful conclusions for the physical understanding of coherence. The analysis of the frequency-dependent coherence information (with 24 hrs time resolution) can be used as a first order approach for classification of surface types.

In Fig. 8.1 the ground-range coherence maps of the Etna test site for L, C, and X-band respectively are depicted. White corresponds to unit coherence, and black corresponds to zero coherence. Lava flows around the volcano, where no or only pioneer vegetation is present, have high coherence in all three frequencies and therefore appear bright. Younger/rougher lava surfaces generate a higher backscattering intensity and therefore have a higher signal-to-noise-ratio than older/smoother lava surfaces. This effect is significant only for short wavelengths on the order of the surface roughness, and is therefore only detectable in X-band and not in the longer wavelength frequencies.

Also a triangular feature having a very low coherence can be seen in the L-band on top of the

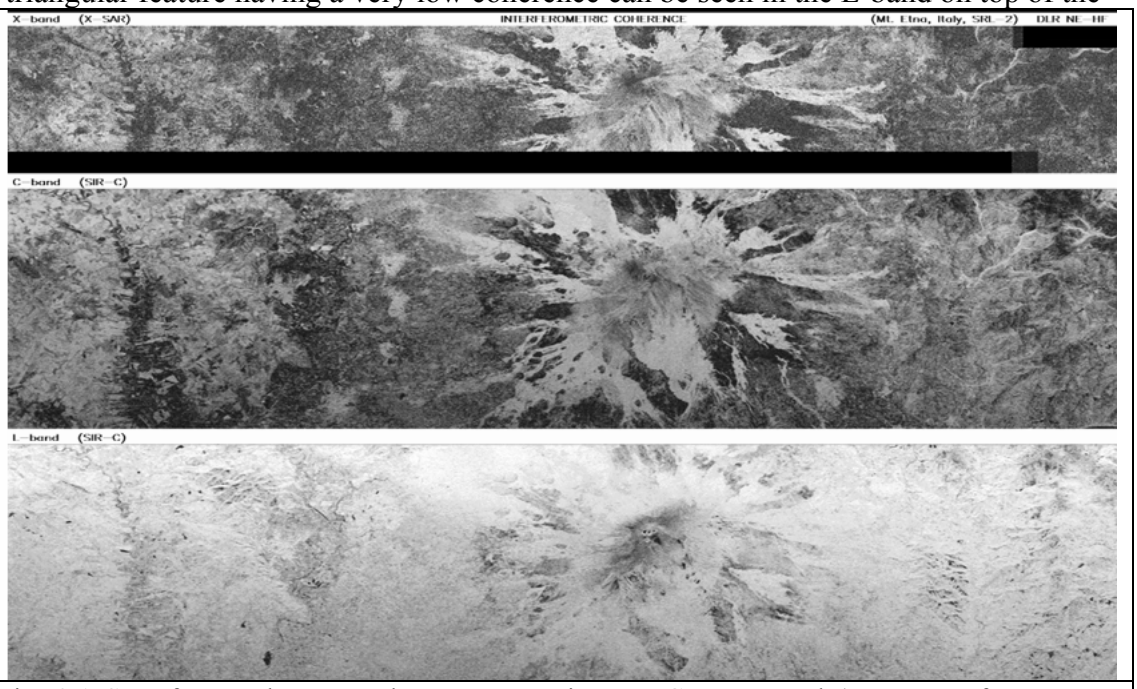

Fig. 9.1 Set of ground range coherence maps in X -, C -, L--Band (sequence from top to bottom), white indicates high coherence black indicates low coherence.

volcano just below the three craters. This feature corresponds to an area covered with fresh volcanic ash. Since this can only be recognized in the larger wavelength L-band it can be assumed that a change in the volume-scattering properties has occurred during the time between the two passes, e.g. due to a change in the volume moisture content, causing the lower coherence. Unfortunately, it was not possible to get detailed information about weather conditions during the mission to verify this assumption.

The forested areas around the volcano are dark in X and C-band and bright in L-band. The reason for this is that short wavelengths in X-band and C-band do not penetrate into the forest volume, and only the backscattering from branches and leaves on the top of the trees is relevant. The movement of the tree branches due to the wind or other influences produces a change in the scatterer geometry and therefore, a degradation in the coherence between the two interferometric images. In the L-band the waves penetrate into the forest volume, and the backscattering is mainly a double bounce from trunks and ground. Therefore, the influence of the scatterer movement in the upper part of the trees is very small, and the coherence is high. The same is valid for agricultural areas around settlements. The settlements, however, have a strong coherence in all three frequencies as expected.

Based on these considerations, empirical rules evaluating the interferometric coherence of different types of natural surfaces in the three frequencies for a first-order classification can be postulated. A schematic representation of a classification algorithm is depicted in Fig.1. The starting frequency for the classification is X-band because this frequency shows a higher sensitivity in its interaction with different surface textures. Depicted in Fig.2 are four different classes surface, each having different coherence values characterized by homogeneous geological and morphological properties:
In dark green, surfaces with $0.10 \leq C \leq 0.40$ with high and dense vegetation but also a part of the fresh ash and scoria mantle (from the 1990's eruptions).
In dark grey, surfaces with $0.40 \leq C \leq 0.55$ with less vegetation and also the ash and scoria mantle with pioneer vegetation.
In yellow, surfaces with $0.55 \leq C \leq 0.65$ with historical lava flows with both pioneer vegetation, ash cover, and a few prehistoric lavas, as well as buildings and other man-made structures.
In orange, surfaces with $0.65 \leq C \leq 1.0$. consisting of historical lava flows with fresh surfaces (mostly less than three centuries old) and a few prehistoric lavas with fresh surfaces (< 30 years).

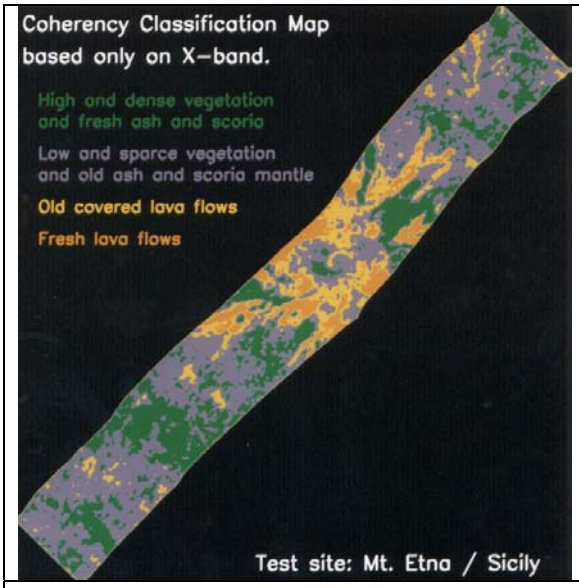

Fig.8.2 Four class coherence map based on X-Band only

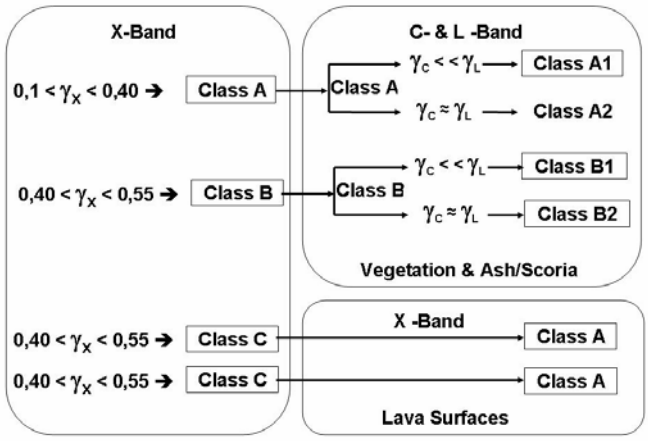

Fig. 8.3 Schematic representation of the interpretation procedure accomplished over the coherence Maps

A very good discrimination can be made in X-band between lava surfaces and the other surface types. Also the discrimination between high and low vegetation is successful. However, the coherence behavior of surfaces covered with fresh ash or fresh scoria and high vegetation, and the coherence behavior of the older ash or scoria mantle and lower vegetation are too similar for discrimination with only one frequency. Further ambiguities are present in the differentiation of prehistoric and historical lavas covered with ash and/or pioneer vegetation. For the elimination of these ambiguities it is necessary to extract information from the other two frequencies.

The coherence difference between X and C-band can be used for evaluation of the ambiguities of the different lava surface types. Lava surfaces covered with pioneer vegetation have a higher coherence

in C-band than in X-band. On the other hand, surfaces without vegetation or ash cover and with very fresh lava has a higher coherence in X-band than in C-band. Using this additional information it is possible to split the last two classes into new, thematic more restricted and homogeneous classes.

The coherence difference between C and L-band reaches a maximum for surfaces with vegetation due to the different penetration capability of these two frequencies. Using the coherence difference between C and L-band, a separation of surfaces with vegetation from surfaces covered with ash and scoria can be made. Using this information we can split each of the first two classes into two new classes.

The result of the classification procedure leads to six classes depicted in Fig. 3:
In dark green, surfaces with $0.10 \leq C \leq 0.40$ in X-band and with a high coherence difference between C and L-band containing now mainly high and dense vegetation. The small part of the ash and scoria fallout deposit of the 1990's eruptions of Etna that is included in this class can by considered as an error due to the inexplicably low coherence of L-band in this region.
In pale grey, surfaces with $0.10 \leq C \leq 0.40$ in X-band and with a low coherence difference between C and L-band containing the majority of the ash and scoria fallout of the 1990's eruptions, and part of the summit craters with fumarolas..
In pale green, surfaces $0.40 \leq C \leq 0.55$ in X-band and with a high coherence difference between Cand L-band containing lower vegetation and agricultural areas, as well as parts of the old ash and scoria mantle with pioneer vegetation.
In dark grey, surfaces with $0.40 \leq C \leq 0.55$ in X-band and with a low coherence difference between C and L-band containing the majority of the ash and scoria mantle without vegetation, lateral scoria cones, and very old lavas with intermittent ash cover. is.
In yellow, surfaces with $0.55 \leq C \leq 0.65$ in X-band. See above. In Fig.3 this class is depicted
In orange, surfaces with a $0.65 \leq C \leq 1.0$ in X-band.

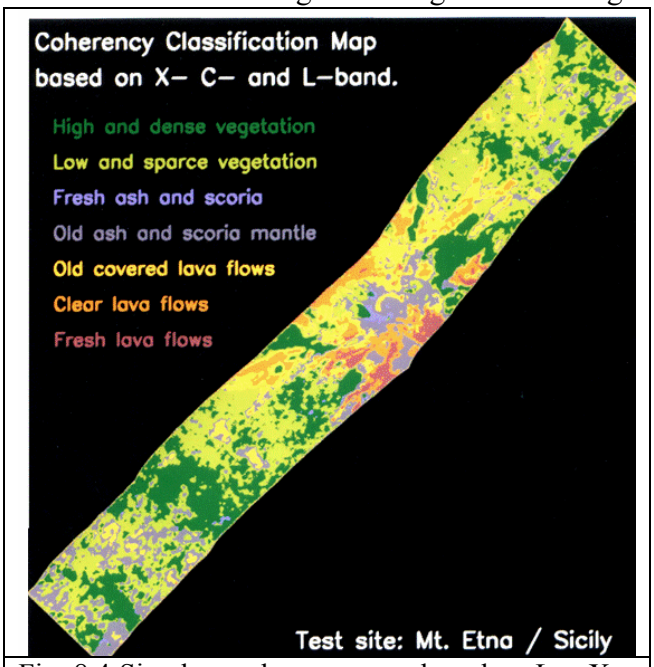

Fig. 8.4 Six class coherence map based on L -, X -, and C –Band as well established using the procedure depicted in Fig. 8.3

It evident that the supervised interpretation approach based on multi frequency multi pass coherence maps is a useful and viable tool for geological characterization.

In particular, the six-class interpretation scheme is effective for distinguishing different volcanic terrains and among vegetated and un vegetated areas. A comparison with the available geological sketch map of Mt.Etna confirmed this result.
The multi pass coherence maps represent a first-order geological interpretation that is very useful for monitoring active volcanoes by means of interferometric SAR. The method is capable to recognize ash and scoria deposits, and lava flows that are produced during the volcanic eruptions. This is very important on the geological point of view.

Reference:
Coltelli M., L Dutra, G. Fornaio, G.Franceschetti, R.Lanari, M. Migliaccio, J. Moreira, K. Papathanassiou, G.Puglisi, D. Riccio, M. Schwäbisch; SIR-C/X-SAR Interferometry over Mt. Etna: DEM Generation, Accuracy Assessment and Data Interpretation,DLR Research Report 95-48, 1996, SSN 0939 - 2963

10. Polarimetric soil roughness and Soil moisture determination

Each target acts as a polarization transformer turning the phase of a scattered wave due to both its special geometry and its electrical properties, conductivity and dielectric constant. The latter in case of the earth surface are dependent normally on the water content of the surface and, therefore, polarization measurements are a very promising tool for the quantitative determination of soil moisture and surface roughness as well.

Several inversion algorithms for the extraction of surface roughness and moisture from polarimetric SAR and scatterometer data have been addressed in the literature. One important class of such algorithms are semi-empirical models which are based on the evaluation of simple amplitude ratios [1],[2]. Both algorithms,[1] and [2], allow the extraction of rms height and volumetric moisture content, without the need of any additional a priori information about the surface characteristics, under the assumption of pure surface scattering. However, these models are mainly valid for a specific range of roughness scales only because the underlying surface scattering model is insufficient and scatterers characterized by multiple scattering effects are not included in the validity domain of the two models.

To establish either new models ore to improve existing -more ore less empirical- models the polarimetric decomposition scattering theory can be used which is presented in the respective lectures of this Lecture Series (Hajnsec et. al.1999).

It has been shown, that the polarimetric eigenvector decomposition technique may be used to overcome these limitations and is able to extend the applicability of the inversion algorithms (Hajnsek et al. 1999). They introduced the 3x3 hermitian positive semidefinite covariance matrix which in general is of rank 3 and the scattering vector as well :

$$[C] = \left\langle \vec{k}\vec{k}^{+} \right\rangle = \begin{bmatrix} \langle |HH|^2 \rangle & \sqrt{2}\langle HHHV^* \rangle & \langle HHVV^* \rangle \\ \sqrt{2}\langle HVHH^* \rangle & 2\langle |HV|^2 \rangle & \sqrt{2}\langle HVVV^* \rangle \\ \langle VVHH^* \rangle & \sqrt{2}\langle VVHv^* \rangle & \langle |VV|^2 \rangle \end{bmatrix} \quad \text{with } \vec{k} = \left[HH, \sqrt{2}HV, VV\right]^T \tag{1}$$

A decomposition of [C] leads to three 3 x 3 independent rank 1 covariance matrices [C_i] as [3]:

$$[C] = \lambda_1 \vec{e_1}\vec{e_1}^{+} + \lambda_2 \vec{e_2}\vec{e_2}^{+} + \lambda_3 \vec{e_3}\vec{e_3}^{+} = [C_1] + [C_2] + [C_3]$$

$$[C_i] = \vec{k_i}\vec{k_i}^{+} \quad \text{with} \quad \vec{k_i} = \lambda_i \mathbf{e_i} = \left[HH_i, \sqrt{2}HV_i, VV_i\right] \tag{2}$$

$\lambda_1 > \lambda_2 > \lambda_3$ are the real non negative eigenvalues of [C] and e_i (i=1,2,3) the corresponding eigenvectors. Eq (2) can be interpreted as the decomposition of the scattering process described by [C] into three orthogonal (independent) elementary scattering mechanisms described by the individual matrices [C_i] [4].

For surface scatterers, (Entropy H < 0.4 and Alpha < 0.40° [4]) the first component [C_1], represents the deterministic anisotropic surface scattering contribution. The second and third components, [C_2] and [C_3] correspond to double-bounce and/or multiple scattering components respectively. In this sense, the $|HH_1|$, $|VV_1|$, and $|HV_1|$ values represent the scattering amplitudes corresponding to the surface scattering only. The disturbing double-bounce (if present) and multiple scattering effects affecting the original |HH|, |VV|, and |HV| have been filtered out.

This theory has been validated using the fully polarimetric L-Band data, acquired by the experimental airborne SAR system of DLR in August 1997 from the Elbe river test-site (Germany) where intensive and extended ground truth measurements have been performed.The estimated volumetric soil moisture content,

from the original amplitudes, using the model proposed in [1], are shown in Fig. 1. The corresponding values, estimated after applying the decomposition are shown in Fig. 5. Apart of the larger number of valid fields, the estimated mv values in Fig.2 correlate better and show a smaller standard deviation than in the original data.

These results allow the conclusion, that the eigenvector decomposition of the covariance matrix improves significantly the performance of roughness and soil-moisture inversion algorithms based on the evaluation of amplitude ratios. On the one hand, it allows to extend drastically the applicability of the algorithms on a larger class of natural surfaces. On the other hand, it leads to an improvement of the roughness and soil-moisture estimates. But, even if the main problems of both algorithms becomes partially weaker, they are still remaining, making the estimation of soil parameters only under "idealised" conditions possible.
Based on these results soil moisture and roughness maps can be established as depicted exemplary in Fig 3 and Fig. 3a

REFERENCES
This section is mainly an extract of Hajnsek I., K. P. Pappathanassiou, A. Reigber, S. R. Cloude: Soil-Moisture Estimation Using Polarimetric SAR Data; Proc IGARSS 1999,
[1] Y. Oh, K. Sarabandi and F.T. Ulaby, "An Empirical Model and an Inversion Technique for Radar Scattering from Bare Soil Surfaces", IEEE Transactions on Geoscience and Remote Sensing, vol. 30 no.2, pp. 370-381, 1992.
[2] P. C. Dubois and J.J. van Zyl, "An Empirical Soil Moisture Estimation Algorithm Using Imaging Radar", IEEE Transactions on Geoscience and Remote Sensing, vol. 33, no. 4, pp. 915-926, 1995.
[3] S. R. Cloude and E. Pottier,"A review of Target Decomposition Theorems in Radar Polarimetry", IEEE Trans. on Geoscience and Remote Sensing,Vol. 34, No. 2, pp. 498 518, 1996.
[4] S. R. Cloude and E. Pottier, "An Entropy Classification Scheme for Land Applications of Polarimetric SAR Data", IEEE Trans. on Geoscience and Remote Sensing, Vol. 35, No. 1, pp. 68-78, 1997.
HAJNSEK, I., CLOUDE, S. R., LEE, J. S. & POTTIER, E., 'Terrain Correction for Quantitative Moisture and Roughness Retrieval Using Polarimetric SAR Data', *Proceedings IGARSS'00*, Honolulu, Hawaii, pp. 1307-1309, July 2000.
CLOUDE, S. R., HAJNSEK, I. & PAPATHANASSIOU, K. P., 'An Eigenvector Method for the Extraction of Surface Parameters in Polarimetric SAR', *Proceedings of the CEOS SAR Workshop*, Toulouse 1999, ESA SP-450, pp. 693 – 698, 1999.

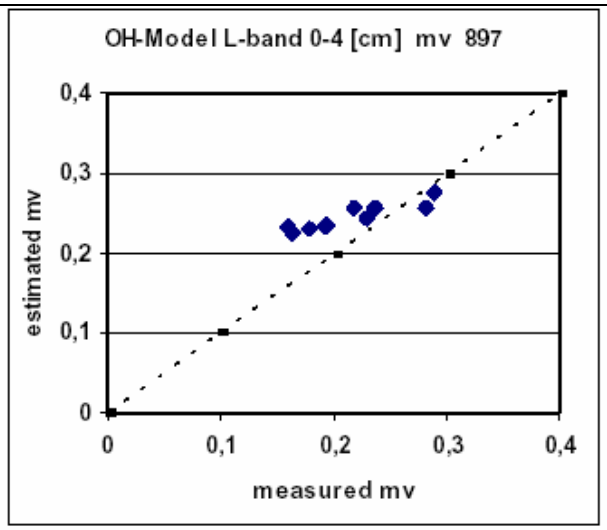

Fig 10.1 With polarimetric decomposition extracted versus measured soil moisture (mv)

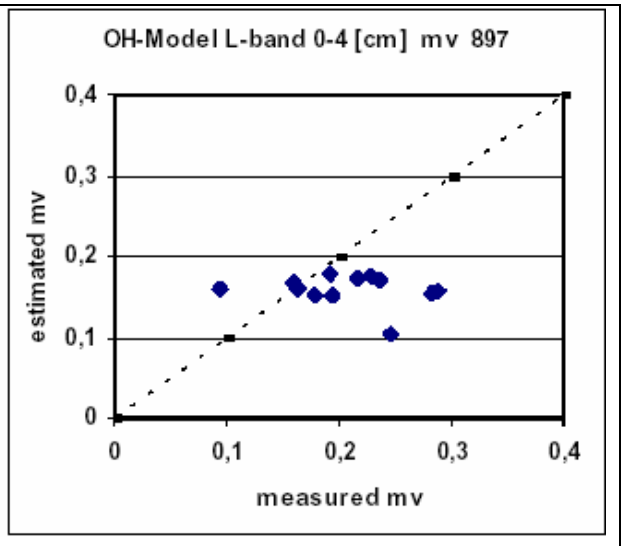

Fig. 10.2 With OH-Model extracted versus measured soil moisture (mv)

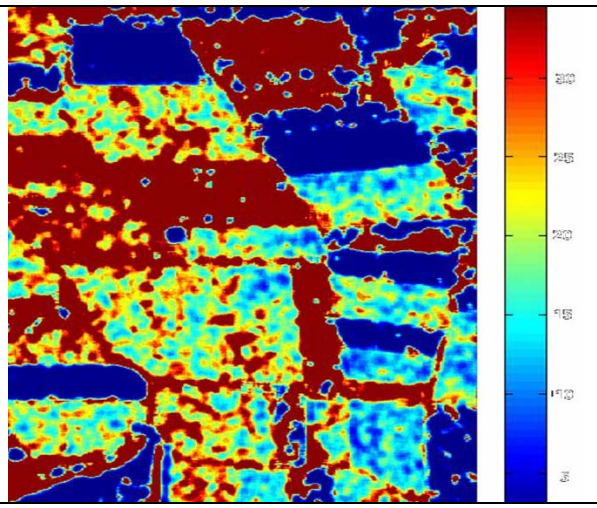

Fig. 10.3a Volumetric Soil Moisture Map *mv* [vol. %](Hajnsek et. al. 2000)

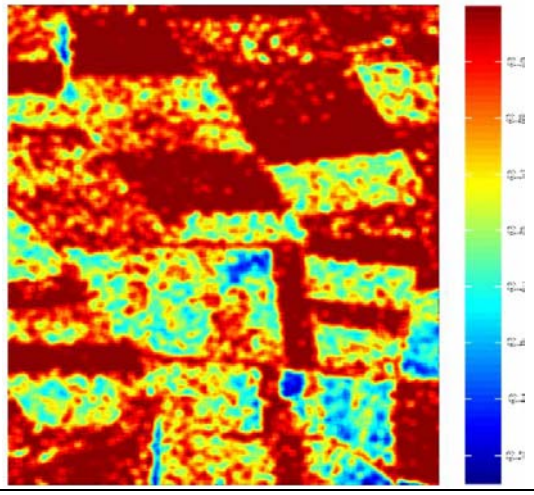

Fig. 10.3b Soil surface roughness Map *ks* (Hajnsek et. al. 2000)

11. Concluding Summary

This application Lecture is a trial to cover interesting areas of the use and application of both SAR Polarimetry and SAR Interferometry by presenting single mostly modern and innovative examples. Chapter 3 is related to applications of Polarimetry for the improvement of ScanSAR technique, chapter four is related to forest applications of the novel Tomography technique which can open the door for a wide field of applications also for military user which have a need for foliage penetration and detection of targets hidden under vegetation: The results in chapter 5 show the tremendous accuracy which can be used in principle for disaster forecasting as well as for applications in scientific an commercial Geology. Building determination, presented in chapter 6, has benefits for urban planning as well as for security manager and, many other commercial, official and scientific groups. But this is the case with all presented examples. The knowledge of ocean currents has tremendous application potential for officials, commercial users, and scientists as well. Traffic monitoring exemplary shown in chapter 8 is indispensable for our society. Surface and vegetation monitoring by means of coherence is a practical way to monitor active volcanoes to recognize ash and scoria deposits that areproduced during volcanic emotions. Chapter ten, last but not least is related to an extremely wide family of communities reaching from farmers over dyke observers even to military user. This points out the importance of Polarimetry and Interferomctry for our society.